Critical Current Density Limitation of LLZO Solid Electrolyte: Microstructure vs Interface

Thibaut Dussart, Nicolas Rividi, Michel Fialin, Gwenaëlle Toussaint, Philippe Stevens, Christel Laberty-Robert

Critical Current Density Limitation of LLZO Solid Electrolyte: Microstructure vs Interface

Journal of The Electrochemical Society, 2021 **168** 120550

Critical Current Density Limitation of LLZO Solid Electrolyte: Microstructure vs Interface

Thibaut Dussart,[1,2] Nicolas Rividi,[3] Michel Fialin,[3] Gwenaëlle Toussaint,[1] Philippe Stevens,[1] and Christel Laberty-Robert[2,4,z]

[1]*EDF R&D, LME department, Moret-sur-Loing, France*
[2]*Laboratoire de chimie de la matière condensée de Paris, Sorbonne Université, Paris, France*
[3]*Service Camparis, Sorbonne Université, Paris, France*
[4]*Réseau sur le Stockage Electrochimique de l'Energie, Amiens, France*

Al-doped $Li_7La_3Zr_2O_{12}$ (LLZO) solid electrolyte is a promising candidate for all-solid-state lithium battery (ASSB) due to its high ionic conductivity and stability against lithium metal. Dense LLZO pellets were prepared by high-temperature sintering and a Li_3BO_3 melting agent was used to control the microstructure (grain size and grain boundary chemistry). An ionic conductivity of 0.49 mS·cm^{-1} was measured at room temperature. The LLZO/Li interface was modified by introducing an aluminum layer. The impact of the microstructure of LLZO ceramics and the chemistry of the LLZO/Li interface were discussed by measuring the critical current density (CCD). Even though secondary phases at the grain boundary lead to an increase of the electronic conductivity, no significant influence of the microstructure on the CCD value (50 μA·cm^{-2}) has been established. The low CCD value has been improved by forming an Al-Li alloy interlayer at the LLZO/Li interface, due to a better homogenization of the Li current at the interface. In parallel, the applied pressure (0.09 MPa vs. 0.4 MPa) has been studied and did impact the CCD. A value of 0.35 μA·cm^{-2} was measured. These results highlight the conditions needed for keeping a good electrolyte/Li interface during the cycling of a solid state battery.

 [DOI: 10.1149/1945-7111/ac44be]

Manuscript submitted September 21, 2021; revised manuscript received December 17, 2021. Published December 30, 2021.

Supplementary material for this article is available online

Since the commercialization of the first Li-ion battery by Sony in 1991, significant efforts have been made to increase their energy density. However, the energy density of the conventional Li-ion technology is limited by the graphite negative electrode which can be replaced by a lighter lithium electrode whose theoretical capacity is 3860 mAh.g^{-1}, more than ten times higher than graphite.[1] The use of a lithium electrode in a conventional Li-ion battery leads to an unstable solid electrolyte interface (SEI) and short-circuits are observed when lithium dendrites grow during plating which penetrates the polymer separator.[2] Solid electrolytes can facilitate the use of the metallic lithium electrode and overcome the safety issues related to the flammability of conventional organic liquid electrolytes.[3] Numerous inorganic solid electrolytes have been reported such as NASICON-type,[4] argyrodite,[5] and cubic garnet-type $Li_7La_3Zr_2O_{12}$ (LLZO).[6] The LLZO solid electrolyte has a high ionic conductivity,[7] a wide potential window,[8] and good stability against lithium,[9] which makes it a good candidate for practical all-solid-state lithium battery (ASSB).

Li garnets can crystalize in two polymorphs: a cubic phase ($Ia\bar{3}d$) which has a conductivity of 10^{-4}–10^{-3} S·cm^{-1}, two orders of magnitude higher than the tetragonal phase ($I4_1/acd$).[6,10] The cubic phase can be stabilized by a partial aliovalent substitution (such as Al^{3+}) of Li^+ in the LLZO structure.[11] The critical current density (CCD) is the highest current density before dendrites grow to produce a short circuit. Reported values of CCD for LLZO range from 46 μA·cm^{-2} to 500 μA·cm^{-2} at room temperature and low stack pressure.[12,13] Even though LLZO is stable against lithium, a high area specific resistance (ASR) has been observed due to the low wettability of LLZO by lithium.[14] The presence of Li_2CO_3 on the LLZO surface has been proposed as a possible reason for this low wettability.[15,16] Nevertheless, Zheng et al. have shown that lithium can wet a Li_2CO_3 pellet and they have pointed out the role of surface impurities on the lithium surface.[17] It has also been reported that the LLZO microstructure has an impact on the ASR. Indeed, Cheng et al. have shown that samples with small grains (20–40 μm) exhibit a lower ASR (37 Ω·cm^2) compared to those with larger grains (100–200 μm) which have an ASR of 130 Ω·cm^2.[12] They estimated a CCD of 134 μA·cm^{-2} and 46 μA·cm^{-2} for the small and large grain samples respectively, indicating a possible impact of the grain morphology on the performances. This may be related to the surface roughness, as it has been shown in.[18] During the high temperature sintering of the samples, a $LiAlO_2$ phase has been observed and it is believed that this phase acts as a melting agent and helps the densification.[19,20] Recently, the higher electronic conductivity of LLZO (10^{-8}–10^{-7} S·cm^{-1}) compared to LIPON (10^{-15}–10^{-12} S·cm^{-1}) has also been proposed as one of the causes of the lithium dendrite propagation by facilitating lithium metal deposition inside the electronically conducting grain boundaries.[21] By changing the grains size, the chemistry of the grain boundary may vary and have an impact on the electronic conductivity. To decrease the ASR and increase the CCD, coatings of lithiophilic oxides or reactive metals towards Li (e.g. Al_2O_3, ZnO, Au, Al) on the LLZO surface have been used.[13,22–24] Even if improvements have been made in terms of CCD, the cause of lithium dendrite growth in LLZO solid electrolyte is still not fully understood.

Contrary to previous works which study separately the impact of the microstructure of a densified LLZO pellet and the Li/LLZO interface, in this paper we studied the dendrite formation via the modification of the chemistry of the Li/LLZO interface and the grain boundaries of a densified LLZO pellet. The objective was to define which of the two factors is preponderant on the formation of dendrites. To do so, we modified the composition at the grain boundaries via the addition of Li_3BO_3 and the Li/LLZO interface by adding a thin layer of Al. To discuss the formation of dendrites via the measurement of the CCD, we studied the structure and the microstructure by SEM and XRD analyses of the LLZO pellets and we have estimated the electronic conductivity at the grain boundaries by impedance spectroscopy. Our results show that the formation of dendrites seems to be mainly influenced by the Li/LLZO interface chemistry. In particular, the nucleation growth processes and indirectly the dendrite formation is controlled by the chemistry and the applied pressure.

[z]E-mail: christel.laberty@sorbonne-universite.fr

Experimental

$Li_{6.76}Al_{0.24}La_3Zr_2O_{12}$ was synthesized via the citrate-nitrate route. Nitrate precursors ($LiNO_3$, sigma Aldrich, 99,99% trace metal basis; $Al(NO_3)_3.9H_2O$, ACS reagent, ⩾98%; $La(NO_3)_3.xH_2O$, 99,9% trace metals basis) and zirconium propoxide (merck, 70 wt. % in 1-propanol) were mixed in EtOH at 40 °C. A 10 wt% excess of $LiNO_3$ (sigma Aldrich, 99.99% trace metals basis) was added to compensate for the lithium loss during the heat treatment. A citric acid (sigma Aldrich, ACS reagent, ⩾99.5%)/ethylene glycol (sigma Aldrich, anhydrous, 99.8%) solution in EtOH was then added and the resulting solution was kept under vigorous stirring for 2 h. The cations/citric acid and citric acid/ethylene glycol ratios were 1/1 and 2/1 respectively. The solvent was then evaporated by increasing the temperature to 80 °C until a viscous gel was obtained. The gel was dried at 120 °C overnight. The dried gel was ground using a pestle and mortar and calcined in air at 900 °C for 12 h in an alumina crucible inside a muffle furnace. The as-synthesized Al-LLZO powder was ball milled at 500 rpm with 3 mm zirconia balls using isopropyl alcohol (IPA) as the liquid medium for 6 h. The powder/balls and powder/IPA ratios were 1/10 and 1/2, respectively. For the sample with the melting agent, 5 wt% Li_3BO_3 (merck, anhydrous, puriss. p.a., ⩾98%) was added to the Al-LLZO powder during the ball milling step. The milled powder was subsequently pressed into 13 mm pellets. These pellets were then sintered in air at 1150 °C for 12 h in a closed alumina crucible inside a muffle furnace. To limit the lithium loss during the heat treatment, the pellets were buried in the mother powder (Al-LLZO). For the 5 wt% Li_3BO_3 sample, the pellets were kept at 780 °C (melting temperature of the sintering aid) for 5 h before heating to the 1150 °C final temperature. The pellets were polished using sandpaper and an oil-based diamond suspension to obtain a mirror-like finish. The relative density values were determined by Archimede's method in IPA and by using the geometric dimension ($\sim$ 1 mm thick pellet, S = 0,85 cm^2) and mass.

Powder X-ray diffraction (XRD) patterns of powders and pellets were recorded using a Bruker D8-Advance diffractometer with Cu-K_α radiation source equipped with a LynxEye detector. XRD data analysis was performed using FullProf software. To investigate the pellet morphology, imaging and microanalysis were performed on a Su-70 Hitachi FEG − SEM fitted out with an X-Max 50 mm^2 Oxford EDX spectrometer. The acceleration voltage was 20 kV. The LLZO/Li interface has been observed using a Hitachi S-3400N scanning electron microscope (SEM) with a 5 kV acceleration voltage. The LLZO pellets were also observed with a CAMECA SX100 electron microprobe at CAMPARIS, Centre National de la Recherche Scientifique, Paris, France. La, Zr, Al, B, and O were analyzed. The analytical setup was: 15 kV, 4 nA current, and 1 μm spot size. Acquisition time was 2 s/elements.

Gold electrodes (50 nm) were sputtered on each face of the 2 mm thick, 13 mm diameter pellet (Q150R ES, Quorum Technologies) for conductivity measurements. A 10 nm thick aluminum layer (Al) was sputtered using the same device to react with the Li disk that was then added to make an alloy and was used as non-blocking electrodes. XPS experiment was performed to check the nature of the Al layer. The Li will react with Al as a change in color is observed. Finally, the roughness of the interface between the LLZO and the LLZO/Al pellets is the same and this parameter will not take into account for the discussion of the Li/LLZO interface discussion. Impedance spectroscopy measurements were carried out using a 1260 Solartron FRA device between 10^7 Hz and 0.1 Hz with a 50 mV amplitude. This value is low to allow an electrochemical reaction between lithium ions and gold. Thus, the impedance response at low frequency translates a charge accumulation/depletion at the electrolyte/electrode interface. Data quality was evaluated using the Lin-KK Tool.[25–28] DRT analysis was performed using the MATLAB toolbox DRTtools.[29] The electronic conductivity was calculated by the polarization technique: a 0.2 V DC voltage was applied on the Au/LLZO/Au cells until a steady-state current was reached.

Galvanostatic cycling was employed to evaluate the critical current density (CCD). The symmetric cells were assembled in a Swagelok-type cell. The contact pressure of 90 kPa was maintained with a spring. The starting current density was 25 $\mu A{\cdot}cm^{-2}$ and the current was subsequently ramped by 25 $\mu A{\cdot}cm^{-2}$ steps. The plating and stripping were performed for 30 min and separated by a rest period of 5 min.

Results and Discussion

The diffraction pattern (Fig. S1 (available online at stacks.iop.org/JES/168/120550/mmedia)) of the as-synthesized Al-LLZO powder exhibits a majority cubic garnet structure with trace impurities (tetragonal phase, $La_2Zr_2O_7$, Li_2ZrO_3, $Li_6Zr_2O_7$). For the cubic structure, the lattice parameter was determined to be 12.981(2) Å, which is consistent with the literature.[20,30] To obtain two different microstructures, the first as-synthesized powder was pressed onto a pellet and then sintered without additive and the second as-synthesized powder was mixed with Li_3BO_3 additive (5 wt%), pressed, and then sintered. XRD patterns of sintered samples are given in Figs. S2 and S3. Both samples exhibit a cubic garnet structure and traces of Li_2ZrO_3. In the case of the 5 wt% Li_3BO_3 pellet, a $La_2Zr_2O_7$ secondary phase has also been identified. The lattice parameter of the 0 wt% Li_3BO_3 and the 5 wt% Li_3BO_3 samples are 12.965(4) and 12.963(5) Å respectively. After the sintering, the lattice parameter has decreased due to Al occupancy in Li sites. The addition of the melting agent does not change the structural parameters of the LLZO and similar lattice parameters have been reported in the literature for sintered LLZO.[31] The final sintered pellet density is 86% and 93% for the 0 wt% Li_3BO_3 and 5 wt% Li_3BO_3 samples, respectively. This confirms that Li_3BO_3

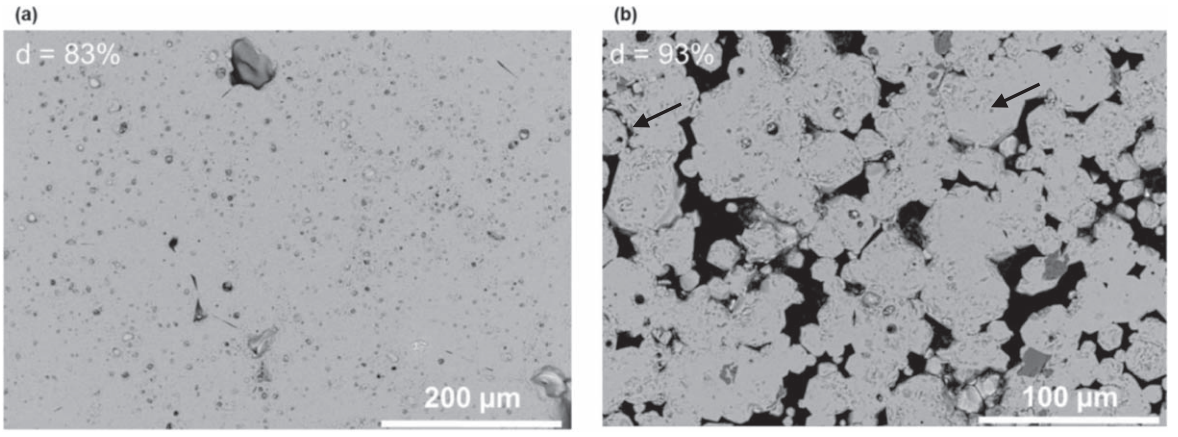

Figure 1. (a) SEM images of the 0 wt% Li_3BO_3 and (b) 5 wt% Li_3BO_3 samples.

helps to increase the final pellet density but leads to the formation of the $La_2Zr_2O_7$ secondary phase.

As shown in Fig. 1, back-scattered electrons (BSE) images indicate two different microstructures. The pellet without the Li_3BO_3 additive exhibits large grains of approximately 150 μm with inter and intragrain porosity whereas the pellet sintered with Li_3BO_3 exhibits two populations of smaller grain sizes (6 μm and 75 μm). Both samples show secondary phases in the intergrain region indicated by the contrast. Indeed, a darker contrast can be explained by a phase made of lighter elements than the grain. An aluminum distribution can be observed at the grain boundary and this phase has been identified on the EDS map as shown in Fig. 2. The dark region has been associated with an Al-rich and O-rich phase, probably $LiAlO_2$, which segregates at the grain boundaries.[19] Nevertheless, no $LiAlO_2$ phase was detected by XRD and this can be explained by a low amount of $LiAlO_2$ compared to the bulk LLZO or its amorphous character. XRD analysis shows that the lattice parameter of the cubic LLZO phase was the same for the two samples with or without LBO but slightly different from the initial powder and EDS analysis indicates the presence of an aluminum phase in both samples. A reaction between aluminum and lithium occurs without perturbing the formation of the LLZO phase as the condition for pellet densification used a bed of powder of initial composition deposited on the ceramic. Nevertheless, the presence of the $LiAlO_2$ phase at the grain boundary should decrease the electronic conductivity leading then to higher current density values as demonstrated in Ref. 32. Other Zr-rich and La-rich secondary phases have been observed between the grains which might correspond to $La_2Zr_2O_7$ and Li_2ZrO_3,[33,34] as seen in the XRD patterns.

The boron distribution has been analyzed by electron microprobe analysis (EMA) mapping as shown in Fig. S4 and is seen to be distributed along the grain boundaries as previously hypothesized, to probably form an amorphous phase as no B-rich phase was identified in the XRD patterns.[35] Finally, the addition of Li_3BO_3 helps to increase the final pellet density, avoid particle growth during the sintering process, and to modify the chemistry of the grain boundaries.

Impedance spectroscopy has been employed to study the transport properties of the LLZO pellets. The Nyquist plot of the 0 wt% Li_3BO_3 pellet at 25 °C is shown in Fig. 3a. Two semi-circles at high and middle frequency are fitted with two R-CPE in series with capacitance values of 2×10^{-11} F and 3×10^{-8} F, respectively. The first semi-circle at high frequency has been associated with the bulk response as the capacitance value lies in the range associated with a bulk phenomenon. The semi-circle at the middle frequency with a capacitance value of 3×10^{-8} F might correspond to the grain boundary or a surface layer.[36] To clarify the nature of the middle frequency arc, Li foil was melted onto each side of the Au coated pellet at 250 °C in an Argon-filled glove box to make an Au-Li alloy interface with the non-blocking electrode. In this configuration, the high-frequency Nyquist plot exhibits the same behavior as the one observed for pure Au blocking electrodes. We observed three main responses (high, middle, and low frequency). The high-frequency responses are comparable in terms of capacitance (2×10^{-11} F) and the impedance can be attributed to the bulk response (Fig. 3b). At low frequency, the depressed arc is associated with two R-CPE elements in series with capacitance values of 8×10^{-9} F and 3×10^{-8} F, respectively. To attribute the other contributions, the

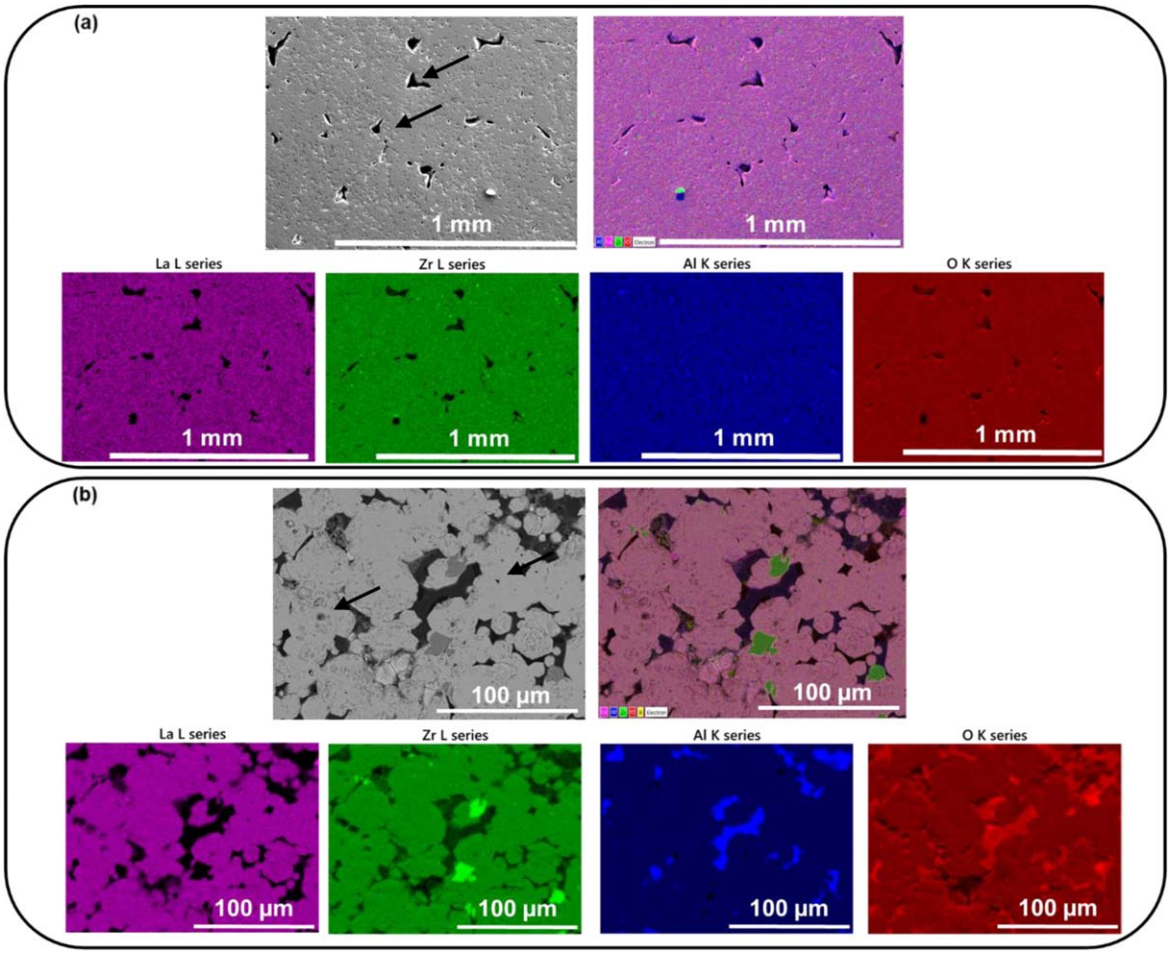

Figure 2. EDS mapping of (a) the 0 wt% Li_3BO_3 (b) 5 wt% Li_3BO_3 samples. (Arrows points intra and inter grain porosities).

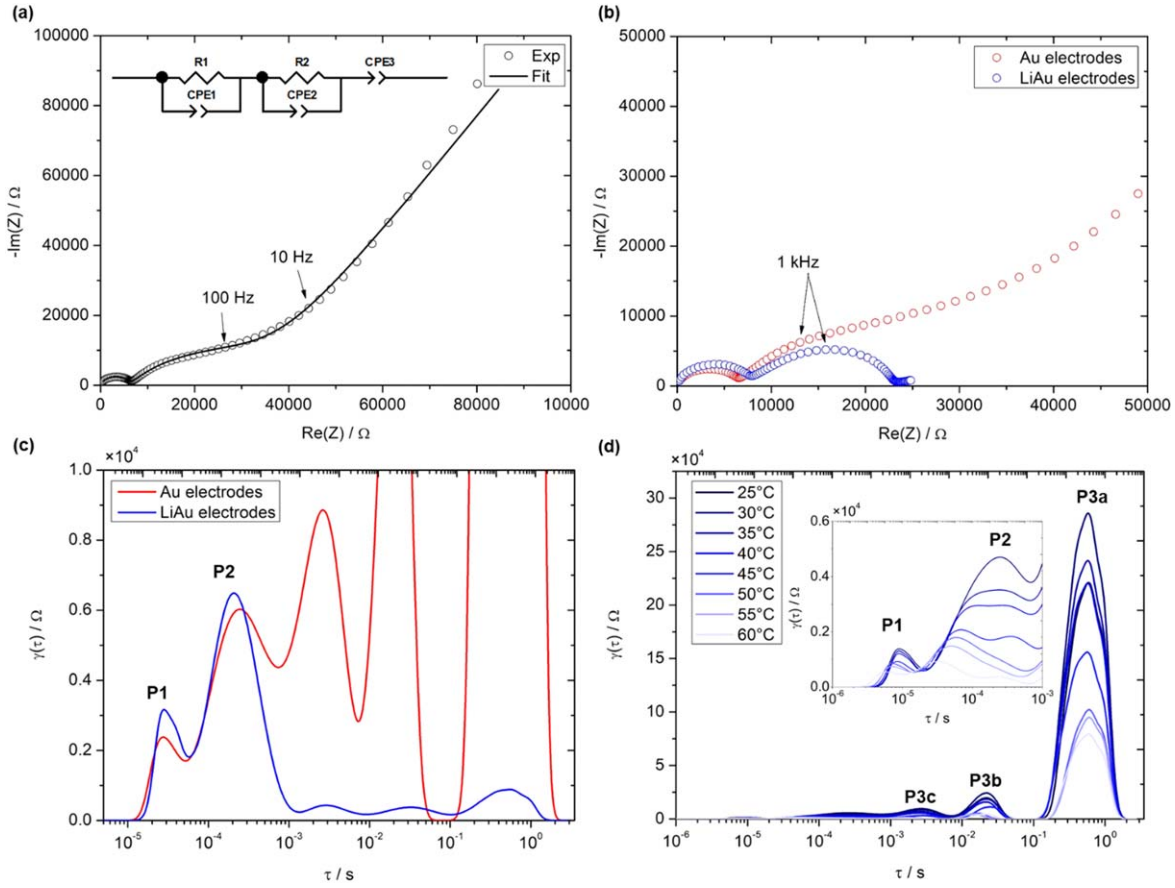

Figure 3. (a) Nyquist plot of the 0 wt% Li_3BO_3 sample with the corresponding equivalent circuit with gold electrodes at 25 °C. A 50 mV excitation amplitude was applied at OCV. The fitted curve is shown as a solid line. (b) Nyquist plot of the 0 wt% Li_3BO_3 sample with gold blocking (red) or lithium non-blocking (blue) electrodes. (c) Corresponding DRT analysis of the impedance spectra. (d) DRT analysis of the 0 wt% Li_3BO_3 sample with gold electrodes at different temperatures from 25 °C to 60 °C. Inset shows the low time constants.

distribution of relaxation times (DRT) was used as this approach enables a clear separation of overlapped arcs associated with physical processes with close time constants. Figure 3c shows the normalized distribution function of the impedance spectra for 0 wt% Li_3BO_3 pellet with either Au or Li-Au electrodes. The polarization peaks P1 (1×10^5 Hz) and P2 (3×10^3 Hz) have similar time constants for both electrodes, indicating processes independent of the nature of the electrode. This behavior can be associated with a bulk and a grain boundary response.[36] Moreover, the peaks P1 and P2 shift to a lower time constant when the temperature is increased, indicating faster processes at higher temperatures (Fig. 3(d)). Since the ionic conductivity is thermally activated, we can attribute the high-frequency arc and the middle-frequency arc to the bulk and the grain boundary response. Accordingly, the total ionic conductivity is estimated to be 4.6×10^{-5} S·cm^{-1} at 25 °C. Higher conductivities around 4×10^{-4} S·cm^{-1} have been reported in the past,[37] but these were obtained on denser samples prepared under more difficult conditions with little grain boundary and porosity. The polarization peaks P3 are associated with the electrolyte-electrode interface and electrode processes since the time constants are higher and do not shift with temperature. This value is rather small compared to the one found in the literature. Several reasons may explain this result: i) the poor density of the pellet (83% relative density compared to 95%), ii) the presence of open and closed pores, indeed the relative density estimated from mass and the pellet dimension is lower for both compositions (80% vs. 83% for LLZO without LBO and 90% vs. 95% for LLZO with LBO) ii) the grain boundaries chemistry. A close examination of the grain boundaries by EDS revealed the presence of $LiAlO_2$ which can be highly resistive, without impacting the crystalline structure as cubic phase is detected by XRD.[38] Using the same approach (Fig. S5), the first and the second arc of the 5 wt% Li_3BO_3 pellet impedance plot have been attributed to the bulk and the grain boundary resistance ($\sim 250\Omega$ and $\sim 700\Omega$) with a capacitance of 2×10^{-11} F and 2×10^{-8} F, respectively. A total ionic conductivity of 4.9×10^{-4} S·cm^{-1} at 25 °C is calculated. Impedance spectra of both samples are compared in Fig. 4. The higher ionic conductivity of the 5% Li_3BO_3 sample can be explained by the higher relative density and to the precipitation of secondary phases in the grain boundaries that may affect Li transport.[39–42] The

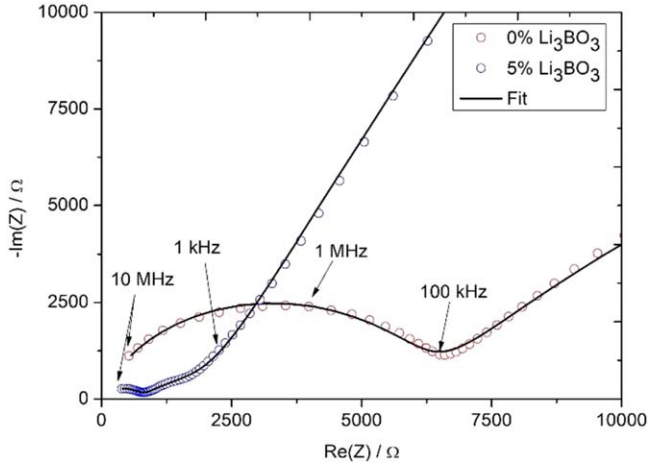

Figure 4. Nyquist plot of the 0% Li_3BO_3 and 5% Li_3BO_3 samples at 25 °C using gold blocking electrodes and a 50 mV excitation amplitude.

impedance of the pellets has been measured as a function of temperature and the activation energy has been calculated from the Arrhenius plot of total conductivities in Fig. 5. Both samples show a similar value of bulk activation energy: 0.34 eV and 0.32 eV for the 0% Li_3BO_3 and the 5% Li_3BO_3 sample respectively, whilst the grain boundary activation energy is much higher for the sample with 5 wt % of Li_3BO_3 (0.74 eV vs 0.57 eV). Here, the presence of Li_3BO_3 changes the conduction mechanism due to the presence of Boron-rich phases. More interestingly, a comparison of the EDS cartography for LLZO with and without LBO shows a difference in the grain boundaries chemistry that may explain this difference. In the sample with LBO, $LiAlO_2$ has been detected with together with $La_2Zr_2O_7$ and Li_2ZrO_3 according to either the XRD and/or EDS analysis. Similar values of bulk activation energies have been obtained in the literature for the cubic garnet structure of LLZO.[6,43] Finally, those values show that introducing secondary phases at the grain boundaries has a significant impact on the lithium ion conduction.

The electronic conductivity of lithium solid electrolyte was also measured since it has been described in the literature as a possible explanation for dendrites formation at relatively low critical current densities.[21] Since the microstructure of LLZO pellets was modified by the introduction of Li_3BO_3 and the presence of secondary phases, the impact of these secondary phases and the grain morphology on the electronic conductivity was evaluated using the polarization technique with two Au blocking electrodes (Fig. S6). Electronic conductivities of 4×10^{-9} S·cm^{-1} and 2×10^{-7} S·cm^{-1} at 25 °C were measured for the 0 wt% Li_3BO_3 and the 5 wt% Li_3BO_3 samples respectively. The values reported in the literature are in the range of 10^{-8} to 10^{-7} S·cm^{-1}.[44,45] The electronic conductivity difference between the two samples is about 2 orders of magnitude. The electronic conduction is therefore greatly influenced by the nature and the composition of the grain boundary and thus we expect a lower critical current density value for the 5 wt % Li_3BO_3 sample.

Literature data also suggest that surface impurities on Li metal foil can lead to a high interfacial resistance, as well as the poor solid-solid contact.[17] First, the chemistry of the LLZO/Li interface was investigated. Each of the faces of a 5 wt% Li_3BO_3 LLZO pellet was rubbed into molten Li to deposit the electrodes. To modify the chemistry of the interface, Li-Al alloy interfaces have also been used. XPS experiment has been performed and indicates the presence of both Al and Al_2O_3 (Fig. S7). As shown in Fig. S8, the Li and Li/Li-Al electrodes bond well to the LLZO surface, and no significant gap has been observed. The formation of the alloy has been confirmed by a color change of the lithium electrode (from metallic grey to dark grey). Areal specific resistances (ASR) can be estimated by dividing the charge transfer resistance by 2 as each interface of the pellet contributes to the overall charge transfer resistance. The ASR values are listed in Table I. The good contact between the 5 wt % Li_3BO_3 sample and pure Li electrode is confirmed by a low ASR of 118 Ω·cm^2. A similar value is obtained with the electrode with the Li-Al interface. The 0 wt % Li_3BO_3 samples show a higher ASR with both electrodes even if the beneficial effect of the Li-Al alloy can be noticed. As described before, the grain size of the 5 wt% Li_3BO_3 sample is smaller than that of the 0 wt% Li_3BO_3 sample. The better interfacial resistance could be linked to the decrease in grain size.[46]

To dissociate the effects of the microstructure and the solid electrolyte|electrode interface, three symmetric cells have been cycled at a different current density at 25 °C: Li|0% Li_3BO_3-LLZO|Li, Li|5% Li_3BO_3-LLZO|Li and Li-Al|5% Li_3BO_3-LLZO|Li-Al. Since it has been previously shown that the ASR value influences the CCD value,[47] we chose to not use the 0% Li_3BO_3—Li electrodes cell for CCD determination. The results from galvanostatic cycling of the symmetric cells are given in Fig. 6. The CDD value is determined when an abrupt voltage drop is observed even if later cycling is stable. We believe that this phenomenon, so-called "soft" short circuits created by resistive short-circuits, could lead to overestimated values of CCD as stable cycling is observed after the soft short occurs.[48,49] A CDD value of 50 μA·cm^{-2} can be estimated for samples with pure Li electrodes regardless of the 5 wt% Li_3BO_3 LLZO pellets. When Li/Li-Al alloy electrodes are used, the CCD value is multiplied by a factor of 2 to reach 100 μA·cm^{-2}. Even if the overall electronic conductivity of the LLZO pellet through grain boundary chemistry is modified, the CCD value is still low and seems to be highly correlated to the nature of the electrode (or the chemistry of the LLZO/electrode interface). Furthermore, lithium self-diffusion in metallic lithium (2.6×10^{-16} m^2.s^{-1} at 50 °C and 9×10^{-15} m^2.s^{-1} at 454 K)[50,51] is much slower than the lithium diffusion coefficient in LLZO (10^{-13} m^2.s^{-1} between 213 K and 253 K).[52] Thus, the Li^+ flux at the interface exceeds the Li^0 flux in lithium and may lead to local overpotentials at the interface. Since the lithium diffusion coefficient in lithium β-LiAl is about 7×10^{-9} m^2.s^{-1},[51] we believe that introducing a metal interlayer that alloys lithium not only helps to decrease the charge transfer resistance at the interface but also provides an intermediate layer regulating the lithium ion flux and electric field during the plating/stripping of lithium and postpones Li dendrites formation.[53–55]

To corroborate the major role of the electrode, a symmetric cell has been assembled and tested under 0.4 MPa stack pressure and a CCD value of 350 μA·cm^{-2} has been obtained (Fig. 7). This value can be explained by the ultralow ASR value of 5 Ω·cm2 (Fig. S9) and by the beneficial effect of the pressure on the LLZO/lithium electrode interface which helps the lithium electrode to restructure

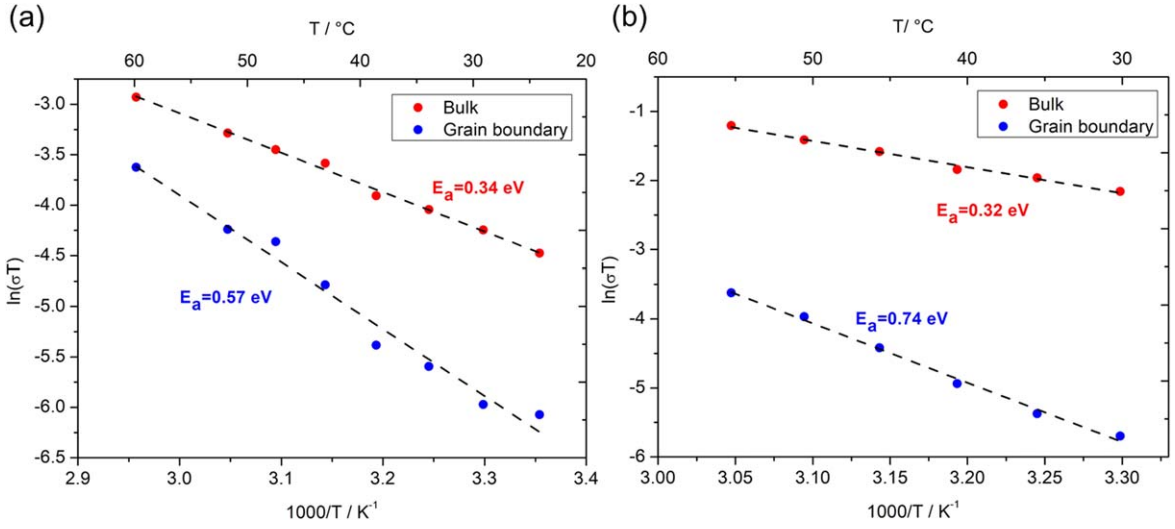

Figure 5. Arrhenius plot of the bulk and grain boundary ionic conductivity of the (a) 0% Li_3BO_3 and (b) 5% Li_3BO_3 samples.

Table I. ASR values of the different samples under an applied pressure of 0.09 MPa.

Sample	ASR/Ω·cm^2 at 25 °C
0% Li_3BO_3—Li electrodes	433
5% Li_3BO_3—Li electrodes	118
0% Li_3BO_3—Li-Al electrodes	321
5% Li_3BO_3—Li-Al electrodes	163

quickly during cycling.[57] As shown in Fig. 8, stable cycling for 140 h has been obtained for the higher pressure cell. The decrease of the overall polarization shown in Fig. 8b has not been attributed to short circuits since no voltage drops have been observed, it might be related to an interface reorganization.[56] Values of ionic and electronic conductivity, ASR, and CCD of all the samples are given in Table II. These results show that the chemistry of the Li/LLZO interface and the pressure applied during cycling are the important parameters for dendrite formation compared to the microstructure of LLZO pellets.

Conclusions

The grain size and grain boundary chemistry of Al-doped LLZO solid electrolyte were modified by Li_3BO_3 addition. Of the two configurations, the highest lithium ionic conductivity of 4.9×10^{-4} S·cm^{-1} at 25 °C was obtained with 5 wt% of Li_3BO_3 in the LLZO pellet. The bulk activation energy of all the samples is similar (0.34–0.32 eV) whilst the activation energy corresponding to the grain boundary ionic conductivity is higher for the 5wt % Li_3BO_3

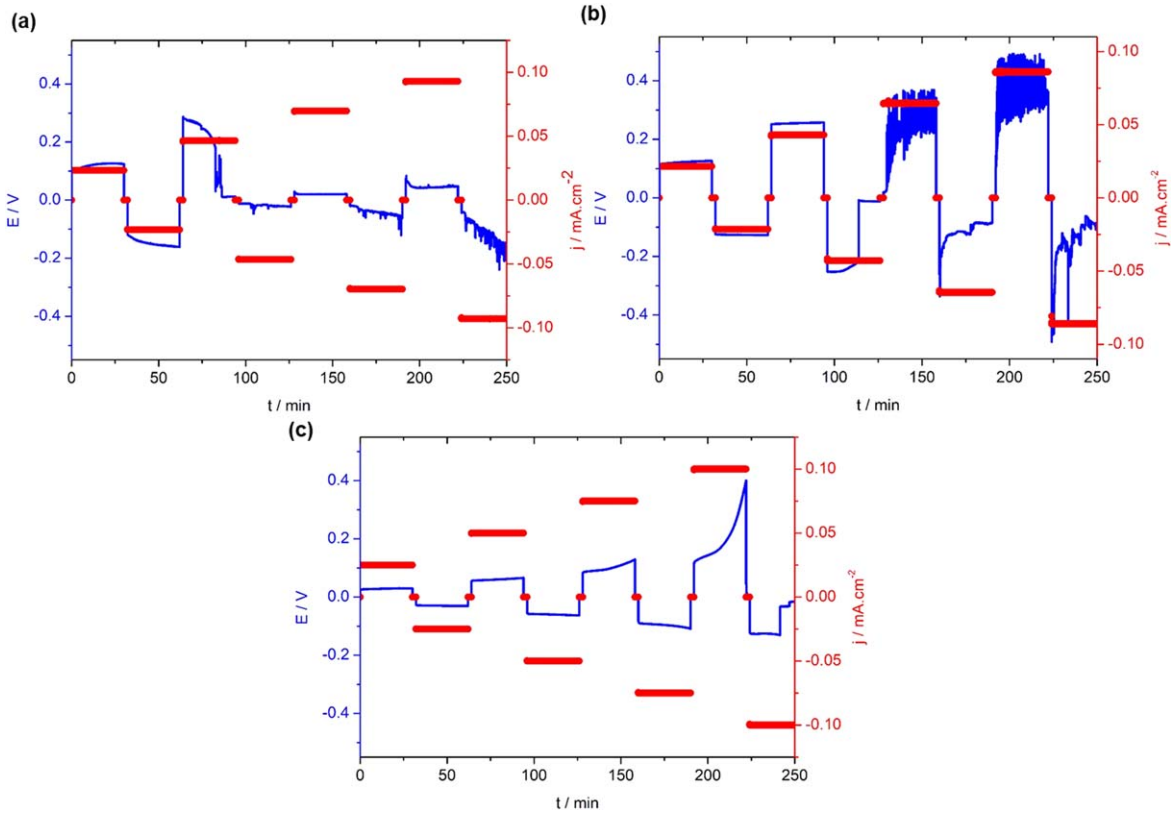

Figure 6. Plating/stripping experiments of the (a) Li|0 wt% Li_3BO_3-LLZO|Li, (b) Li|5 wt% Li_3BO_3-LLZO|Li, (c) Li-Al|5 wt% Li_3BO_3-LLZO|Li-Al symmetric cells at 25 °C under 0.09 MPa stack pressure.

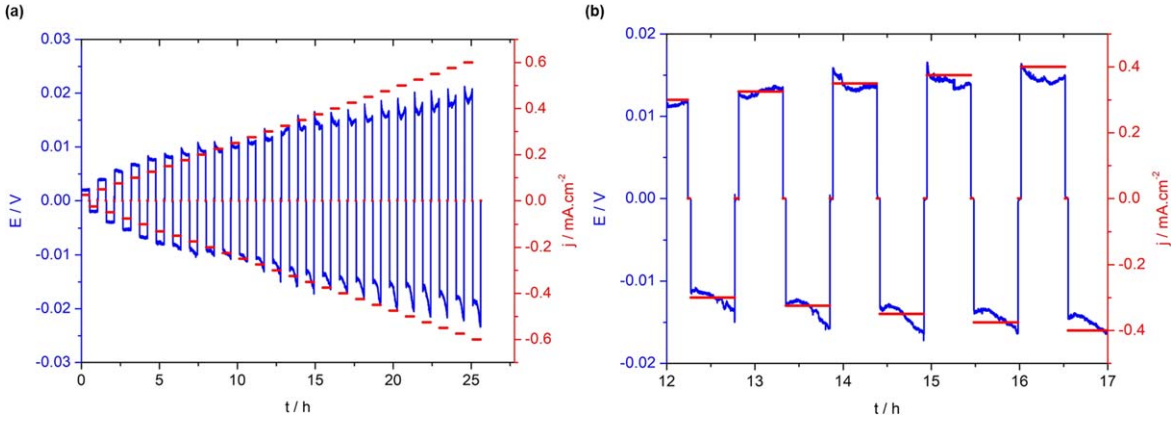

Figure 7. Plating/stripping experiments of the Li-Al|5 wt% Li_3BO_3-LLZO|Li-Al symmetric cells at 25 °C under 0.4 MPa stack pressure. The full test is given in (a) and we assumed a soft short circuit at 0.35 mA·cm^{-2} (b).

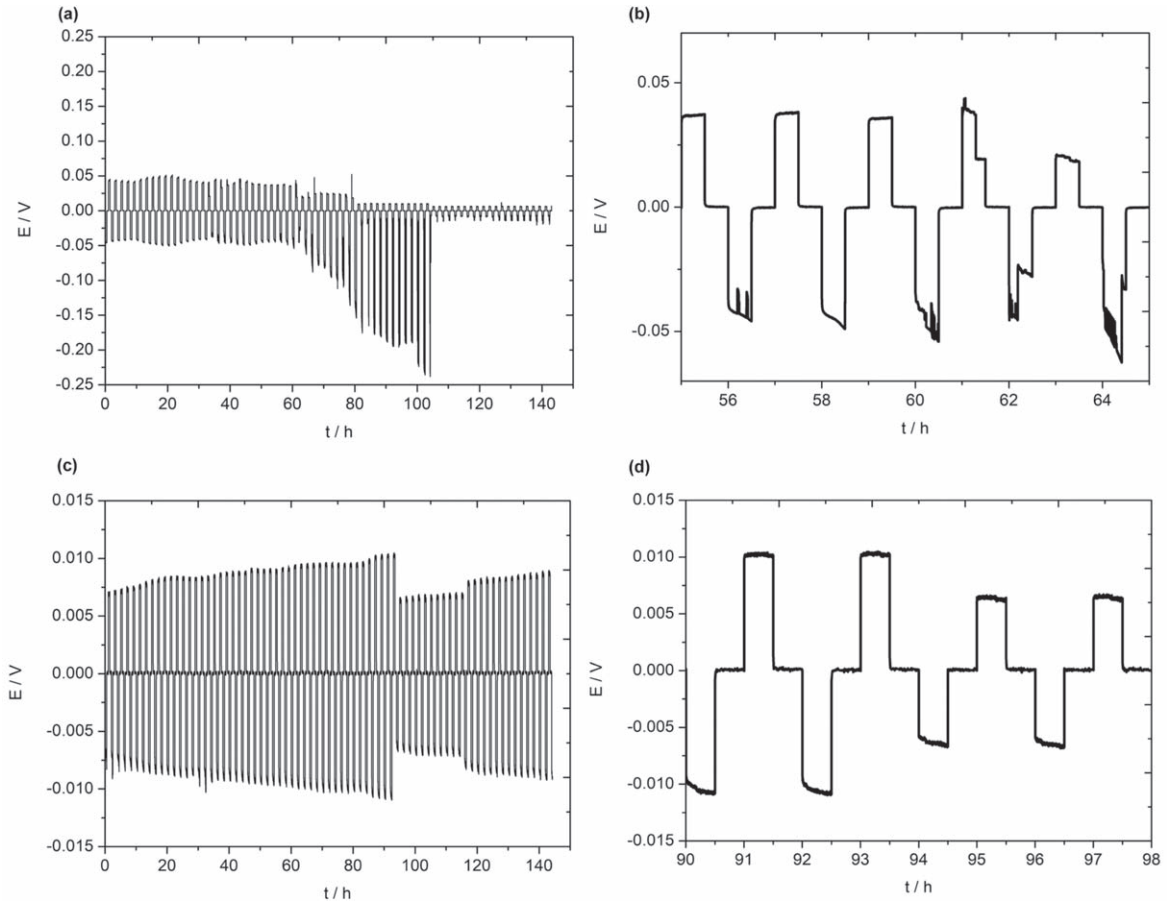

Figure 8. Galvanostatic cycling of the Li-Al|5 wt% Li_3BO_3-LLZO|Li-Al symmetric cells at 25 °C under (a)–(b) 0.09 MPa and (c)–(d) 0.4 MPa stack pressure. A short circuit has been detected after 56 h of cycling for the lower pressure cell (b) whereas a stable cycling has been obtained for 100 h of cycling for the higher pressure cell.

Table II. Summary of ionic and electronic conductivity, ASR, and CCD values of all the compositions.

Sample	$\sigma_{Li+bulk}$/S·cm^{-1}	σ_{Li+gb}/S.cm^{-1}	σ_e_/S·cm^{-1}	Electrodes	P/MPa	T/°C	ASR/Ω·cm^2	CCD/μA·cm^{-2}
0% LBO	3.8×10^{-5}	7.7×10^{-6}	4×10^{-9}	Li	0,09	25	393	50
5% LBO	3.2×10^{-4}	1.7×10^{-4}	2×10^{-7}	Li	0,09	25	158	50
5% LBO	3.2×10^{-4}	1.7×10^{-4}	2×10^{-7}	Li-Al	0,09	25	93	100
5% LBO	3.2×10^{-4}	1.7×10^{-4}	2×10^{-7}	Li	0,09	25	17	—
5% LBO	3.2×10^{-4}	1.7×10^{-4}	2×10^{-7}	Li-Al	0,4	25	5	350

sample in which secondary phases have been identified at the intergrain region. Even though the microstructure of the Li_3BO_3/LLZO solid electrolyte pellets is different, no consequence on the value of the critical current density has been observed. A CCD value of 50 μA·cm^{-2} at 25 °C for samples with or without Li_3BO_3 has been measured for "pure" Li electrodes. The LLZO/lithium interface has been modified by introducing an aluminum interlayer. In this case, a CCD value of 100 μA·cm^{-2} at 25 °C has been obtained. By increasing the applied pressure to 0.4 MPa, an ASR and CCD value of 5 Ω·cm^2 and 350 μA·cm^{-2} have been obtained respectively. These results suggest that the nature of the interface and the chemistry of the lithium electrode play a major role compared to the microstructure of the LLZO solid electrolyte on the electrochemical performance during the plating/stripping test. Finally, these results highlight the importance of a buffer layer between LLZO and Li electrode in increasing the CCD value. We hypothesize that this buffer layer helps to homogenize the Li-concentration at the interface, because of the difference in Li diffusion coefficient in LLZO compared to metallic Li. This finding will impact the design of the LLZO/Li interface for all-solid-state batteries, including those with LLZO as the electrolyte.

Acknowledgments

We thank the ANRT for funding and the Institut des Matériaux de Paris Centre (IMPC FR2482) for servicing FEGSEM & EDX instrumentation and Sorbonne Université, CNRS and C'Nano projects of the Région Ile-de-France for funding.

ORCID

Gwenaëlle Toussaint https://orcid.org/0000-0003-0964-143X
Christel Laberty-Robert https://orcid.org/0000-0003-3230-3164

References

1. J.-M. Tarascon and M. Armand, *Nature*, **414**, 359 (2001).
2. J. B. Goodenough and Y. Kim, *Chem. Mater.*, **22**, 587 (2010).
3. H. Shen, E. Yi, L. Cheng, M. Amores, G. Chen, S. Sofie, and M. Doeff, *Sustain. Energy Fuels*, **3**, 1647 (2019).
4. H. Aono, N. Imanaka, and G. Ya Adachi, *Acc. Chem. Res.*, **27**, 265 (1994).

5. H. J. Deiseroth, S. T. Kong, H. Eckert, J. Vannahme, C. Reiner, T. Zaiß, and M. Schlosser, *Angew. Chemie - Int. Ed.*, **47**, 755 (2008).
6. R. Murugan, V. Thangadurai, and W. Weppner, *Angew. Chemie - Int. Ed.*, **46**, 7778 (2007).
7. D. Rettenwander et al., *Chem. Mater.*, **28**, 2384 (2016).
8. T. Thompson, S. Yu, L. Williams, R. D. Schmidt, R. Garcia-Mendez, J. Wolfenstine, J. L. Allen, E. Kioupakis, D. J. Siegel, and J. Sakamoto, *ACS Energy Lett.*, **2**, 462 (2017).
9. V. Thangadurai, S. Narayanan, and D. Pinzaru, *Chem. Soc. Rev.*, **43**, 4714 (2014).
10. J. Awaka, N. Kijima, H. Hayakawa, and J. Akimoto, *J. Solid State Chem.*, **182**, 2046 (2009).
11. H. Buschmann et al., *Phys. Chem. Chem. Phys.*, **13**, 19378 (2011).
12. L. Cheng, W. Chen, M. Kunz, K. Persson, N. Tamura, G. Chen, and M. Doeff, *ACS Appl. Mater. Interfaces*, **7**, 2073 (2015).
13. C. L. Tsai, V. Roddatis, C. V. Chandran, Q. Ma, S. Uhlenbruck, M. Bram, P. Heitjans, and O. Guillon, *ACS Appl. Mater. Interfaces*, **8**, 10617 (2016).
14. H. Buschmann, S. Berendts, B. Mogwitz, and J. Janek, *J. Power Sources,*, **206**, 236 (2012).
15. L. Cheng et al., *Phys. Chem. Chem. Phys.*, **16**, 18294 (2014).
16. A. Sharafi, E. Kazyak, A. L. Davis, S. Yu, T. Thompson, D. J. Siegel, N. P. Dasgupta, and J. Sakamoto, *Chem. Mater.*, **29**, 7961 (2017).
17. H. Zheng, S. Wu, R. Tian, Z. Xu, H. Zhu, H. Duan, and H. Liu, *Adv. Funct. Mater.*, **30**, 1 (2020).
18. X. Zhang, X. Zhang, Q. J. Wang, K. L. Harrison, S. A. Roberts, and S. J. Harris, *Cell Reports Physical Science*, **1**, 100012 (2020).
19. L. Cheng, J. S. Park, H. Hou, V. Zorba, G. Chen, T. Richardson, J. Cabana, R. Russo, and M. Doeff, *J. Mater. Chem. A*, **2**, 172 (2014).
20. H. El-Shinawi, G. W. Paterson, D. A. MacLaren, E. J. Cussen, and S. A. Corr, *J. Mater. Chem. A*, **5**, 319 (2017).
21. F. Han, A. S. Westover, J. Yue, X. Fan, F. Wang, M. Chi, D. N. Leonard, N. J. Dudney, H. Wang, and C. Wang, *Nat. Energy*, **4**, 187 (2019).
22. X. Han et al., *Nat. Mater.*, **16**, 572 (2017).
23. C. Wang et al., *Nano Lett.*, **17**, 565 (2017).
24. K. K. Fu et al., *Sci. Adv.*, **3**, 1 (2017).
25. B. A. Boukamp, *J. Electrochem. Soc.*, **142**, 1885 (1995).
26. M. Schönleber, D. Klotz, and E. Ivers-Tiffée, *Electrochim. Acta*, **131**, 20 (2014).
27. M. Schönleber and E. Ivers-Tiffée, *Electrochem. Commun.*, **58**, 15 (2015).
28. T. H. Wan, M. Saccoccio, C. Chen, and F. Ciucci, *Electrochim. Acta*, **184**, 483 (2015).
29. I. Kokal, M. Somer, P. H. L. Notten, and H. T. Hintzen, *Solid State Ionics*, **185**, 42 (2011).
30. N. Janani, C. Deviannapoorani, L. Dhivya, and R. Murugan, *RSC Adv.*, **4**, 51228 (2014).
31. Z. Huang, L. Chen, B. Huang, B. Xu, G. Shao, H. Wang, Y. Li, and C. A. Wang, *ACS Appl. Mater. Interfaces*, **12**, 56118 (2020).
32. J. Sakamoto, E. Rangasamy, H. Kim, Y. Kim, and J. Wolfenstine, *Nanotechnology*, **24** (2013).
33. F. M. Pesci, R. H. Brugge, A. K. O. Hekselman, A. Cavallaro, R. J. Chater, and A. Aguadero, *J. Mater. Chem. A*, **6**, 19817 (2018).
34. R. Takano, K. Tadanaga, A. Hayashi, and M. Tatsumisago, *Solid State Ionics*, **255**, 104 (2014).
35. W. B. Reid and A. R. West, *Solid State Ionics*, **28–30**, 681 (1988).
36. P. Braun, C. Uhlmann, A. Weber, H. Störmer, D. Gerthsen, and E. Ivers-Tiffée, *J. Electroceramics*, **38**, 157 (2017).
37. W. Xia, B. Xu, H. Duan, Y. Guo, H. Kang, H. Li, and H. Liu, *ACS Appl. Mater. Interfaces*, **8**(8), 5335 (2016).
38. Y. Kim, H. Jo, J. L. Allen, H. Choe, J. Wolfenstine, and J. Sakamoto, *J. Am. Ceram. Soc.*, **99**, 1367 (2016).
39. J. Gao, S. Shi, R. Xiao, and H. Li, *Solid State Ionics*, **286**, 122 (2016).
40. A. C. Sutorik, M. D. Green, C. Cooper, J. Wolfenstine, and G. Gilde, *J. Mater. Sci.*, **47**, 6992 (2012).
41. I. N. David, T. Thompson, J. Wolfenstine, J. L. Allen, and J. Sakamoto, *J. Am. Ceram. Soc.*, **98**, 1209 (2015).
42. A. Sharafi, C. G. Haslam, R. D. Kerns, J. Wolfenstine, and J. Sakamoto, *J. Mater. Chem. A*, **5**, 21491 (2017).
43. F. M. Pesci, A. Bertei, R. H. Brugge, S. P. Emge, A. K. O. Hekselman, L. E. Marbella, C. P. Grey, and A. Aguadero, *ACS Appl. Mater. Interfaces*, **12**, 32806 (2020).
44. Y. T. Chen, A. Jena, W. K. Pang, V. K. Peterson, H. S. Sheu, H. Chang, and R. S. Liu, *J. Phys. Chem. C*, **121**, 15565 (2017).
45. E. Rangasamy, J. Wolfenstine, and J. Sakamoto, *Solid State Ionics*, **206**, 28 (2012).
46. L. Cheng et al., *ACS Appl. Mater. Interfaces*, **7**, 17649 (2015).
47. F. Flatscher, M. Philipp, S. Ganschow, H. M. R. Wilkening, and D. Rettenwander, *J. Mater. Chem. A*, **8**, 15782 (2020).
48. D. Street, *Electrochim. Acta*, **38**, 1233 (1993).
49. C. Fu, V. Venturi, J. Kim, Z. Ahmad, A. W. Ells, V. Viswanathan, and B. A. Helms, *Nat. Mater.*, **19**, 758 (2020).
50. P. Heitjans, A. Körblein, H. Ackermann, D. Dubbers, F. Fujara, and H.-J. Stöckmann, *J. Phys. F: Met. Phys.*, **15**, 41 (1985).
51. T. Krauskopf, B. Mogwitz, C. Rosenbach, W. G. Zeier, and J. Janek, *Adv. Energy Mater.*, **9** (2019).
52. F. A. García Daza, M. R. Bonilla, A. Llordés, J. Carrasco, and E. Akhmatskaya, *ACS Appl. Mater. Interfaces*, **11**, 753 (2019).
53. A. V. Virkar, L. Viswanathan, and D. R. Biswas, *J. Mater. Sci.*, **15**, 302 (1980).
54. T. Swamy, R. Park, B. W. Sheldon, D. Rettenwander, L. Porz, S. Berendts, R. Uecker, W. Craig Carter, and Y. M. Chiang, *DOE Pages*, **165**, A3648 (2018).
55. F. Aguesse, W. Manalastas, L. Buannic, J. M. L. Del Amo, G. Singh, A. Llordés, and J. Kilner, *ACS Appl. Mater. Interfaces*, **9**, 3808 (2017).
56. M. Wang, J. B. Wolfenstine, and J. Sakamoto, *Electrochim. Acta*, **296**, 842 (2019).
57. T. R. Jow and C. C. Liang, *J. Electrochem. Soc.*, **129**, 1429 (1982).